Radar Characteristics of Supercell Thunderstorms Traversing the Appalachian Mountains

KATHERINE E. MCKEOWN,[a] CASEY E. DAVENPORT,[b] MATTHEW D. EASTIN,[b] SARAH M. PURPURA,[c] AND ROGER R. RIGGIN IV[b]

[a] *The Pennsylvania State University, University Park, Pennsylvania*
[b] *University of North Carolina at Charlotte, Charlotte, North Carolina*
[c] *Verisk Weather Solutions, Lexington, Massachusetts*

(Manuscript received 27 June 2023, in final form 12 February 2024, accepted 20 February 2024)

ABSTRACT: The evolution of supercell thunderstorms traversing complex terrain is not well understood and remains a short-term forecast challenge across the Appalachian Mountains of the eastern United States. Although case studies have been conducted, there has been no large multicase observational analysis focusing on the central and southern Appalachians. To address this gap, we analyzed 62 isolated warm-season supercells that occurred in this region. Each supercell was categorized as either crossing (~40%) or noncrossing (~60%) based on their maintenance of supercellular structure while traversing prominent terrain. The structural evolution of each storm was analyzed via operationally relevant parameters extracted from WSR-88D radar data. The most significant differences in radar-observed structure among storm categories were associated with the mesocyclone; crossing storms exhibited stronger, wider, and deeper mesocyclones, along with more prominent and persistent hook echoes. Crossing storms also moved faster. Among the supercells that crossed the most prominent peaks and ridges, significant increases in base reflectivity, vertically integrated liquid, echo tops, and mesocyclone intensity/depth were observed, in conjunction with more frequent large hail and tornado reports, as the storms ascended windward slopes. Then, as the supercells descended leeward slopes, significant increases in mesocyclone depth and tornado frequency were observed. Such results reinforce the notion that supercell evolution can be modulated substantially by passage through and over complex terrain.

SIGNIFICANCE STATEMENT: Understanding of thunderstorm evolution and severe weather production in regions of complex terrain remains limited, particularly for storms with rotating updrafts known as supercell thunderstorms. This study provides a systematic analysis of numerous warm season supercell storms that moved through the central and southern Appalachian Mountains. We focus on operationally relevant radar characteristics and differences among storms that maintain supercellular structure as they traverse the terrain (crossing) versus those that do not (noncrossing). Our results identify radar characteristics useful in distinguishing between crossing and noncrossing storms, along with typical supercell evolution and severe weather production as storms cross the more prominent peaks and ridges of the central and southern Appalachian Mountains.

KEYWORDS: Complex terrain; Mesocyclones; Supercells; Radars/Radar observations; Operational forecasting

1. Introduction

Anticipating the evolution of deep moist convection is a forecast challenge, particularly in regions of complex mountainous terrain. While supercells are less common across the central and southern Appalachian Mountains (e.g., Gaffin and Parker 2006; Lane 2008), such storms often cause significant damage through a combination of severe wind gusts, large hail, and tornadoes. Supercell events across the region, including the widespread 27–28 April 2011 outbreak (Gaffin 2012; Knupp et al. 2014) and multiple localized events (Keighton et al. 2004; Gaffin and Hotz 2011; Prociv 2012), have demonstrated challenges with both monitoring critical low-level storm structure due to radar beam blockage and limited understanding of how supercells interact with and are modified by complex terrain, including their evolution, longevity, and severe weather production.

Observational case studies of supercells interacting with the Appalachians have highlighted the importance of local terrain shape and configuration relative to both the environmental flow and supercell motion. For example, supercell intensification during passage over a valley has been attributed to local enhancements in potential buoyancy and storm-relative helicity (SRH) caused by the channeling of synoptic-scale flow through the valley (LaPenta et al. 2005; Bosart et al. 2006; Schneider 2009; Gaffin 2012; Knupp et al. 2014; Tang et al. 2016). Likewise, mesocyclone intensifications and tornadogenesis downstream of prominent terrain features are often attributed to leeside vortex stretching (Keighton et al. 2004; Lyza and Knupp 2014), but not all supercells experience leeside intensification (Prociv 2012).

Numerical simulations of supercells interacting with complex terrain have indicated that terrain slope, peak altitude, and orientation relative to the low-level environmental flow can modulate storm intensity by altering the instability and vertical shear in the local environment and enhancing updraft magnitudes. For example, using idealized two-dimensional terrain, Markowski and Dotzek (2011) demonstrated that supercells

Corresponding author: Matthew D. Eastin, mdeastin@charlotte.edu

DOI: 10.1175/WAF-D-23-0110.1

TABLE 1. List of supercell case dates and number of crossing and noncrossing supercells that occurred on each date. The outbreak category denotes cases from 27 to 28 Apr 2011, while the nonoutbreak cases occurred on other dates.

Case date	Crossing cases	Noncrossing cases	Total cases	Category
8 May 2009	3	3	6	Nonoutbreak
9 May 2009	1	0	1	Nonoutbreak
8 Apr 2011	1	0	1	Nonoutbreak
27–28 Apr 2011	9	3	12	Outbreak
11 Apr 2013	0	2	2	Nonoutbreak
28 Apr 2014	2	0	2	Nonoutbreak
27 Jul 2014	4	4	8	Nonoutbreak
9 Apr 2015	4	3	7	Nonoutbreak
25 Apr 2015	0	5	5	Nonoutbreak
25 Jun 2015	0	3	3	Nonoutbreak
28 Apr 2016	0	4	4	Nonoutbreak
1 May 2016	1	9	10	Nonoutbreak
14 Apr 2019	0	1	1	Nonoutbreak
All dates	25	37	62	

tended to strengthen in areas with upslope flow due to increases in low-level humidity and enhanced convective available potential energy (CAPE), while supercells tended to weaken in areas with downslope flow due to decreases in low-level relative humidity and enhanced convective inhibition (CIN). Moreover, the ground-relative wind profile relative to the terrain was critical in determining the regions of upslope and downslope flow that modulated the local environment and storm intensity. Smith et al. (2016), using idealized three-dimensional terrain, demonstrated that terrain-induced blocking of low-level upslope flow enhanced supercell updrafts, which increased hydrometeor density (and graupel/hail production), the areal extent of precipitation (or storm size), and cold pool outflow (providing additional low-level lift). Subsequent simulations using realistic terrain have confirmed these idealized results (e.g., Scheffknecht et al. 2017; Mulholland et al. 2020; LeBel et al. 2021). Furthermore, using High Resolution Rapid Refresh (HRRR) model analyses, Katona et al. (2016) and Katona and Markowski (2021) demonstrated that terrain-induced environmental modulation can be substantial, at times, and thus sufficient to impact storm intensity.

Building upon these limited case studies, Purpura et al. (2023) recently documented environmental characteristics of 62 isolated warm-season supercells passing through the southern and central Appalachians. The supercells were classified as either "crossing" or "noncrossing" based on their maintenance of supercellular structure (e.g., a hook echo or mesocyclone) during interaction with prominent terrain. The prestorm synoptic characteristics common among crossing storms (relative to noncrossing storms) included a stronger polar jet, a deeper trough, a north–south-oriented cold front, a strong prefrontal low-level jet, and no wedge front associated with cold-air damming leeward of the terrain. On the mesoscale, near-storm soundings revealed that crossing storms encountered stronger low-level vertical shear, greater storm-relative helicity, and greater midlevel moisture in the elevated terrain than noncrossing storms. Such results, which are consistent with the prior case studies, support the notion that an environment providing sustained dynamic support for mesocyclones is critical to supercell maintenance when interacting with significant terrain.

In this study, we extend the Purpura et al. (2023) analysis, using the same supercell database, to document the radar-based structure and evolution of multiple crossing and noncrossing supercells interacting with prominent elevated terrain. Given our overall goal of better anticipating supercell maintenance and longevity, and their potential for severe weather production across the southern and central Appalachian region, we wish to assess whether Doppler radar observations can provide useful short-term forecast information. Specifically, do supercells that cross larger-scale terrain features (~50–100 km in width) often exhibit greater radar reflectivities, higher echo tops, or stronger/deeper mesocyclones? What structure, evolution, and severe weather production do supercells exhibit while ascending and descending prominent smaller-scale peaks and ridges (~20–30 km in width) within the terrain system? Additionally, this study will expand and contextualize the limited number of observational case studies and idealized modeling studies of supercell–terrain interactions.

This paper is outlined as follows. Section 2 reviews the supercell database and outlines the methods used to document their structural evolution via Doppler radar. Section 3 outlines our salient results in terms of common radar-based storm parameters by first discussing representative examples of crossing and noncrossing supercells passing over elevated terrain and then providing a statistical comparison between crossing and noncrossing supercells, along with a composite analysis of supercells crossing prominent peaks and ridges. Last, our key findings and avenues for future work are summarized in section 4.

2. Data and methods

a. *Supercell cases*

The supercell database developed by Purpura et al. (2023) was used in this study. The database consists of 62 isolated warm-season supercells that moved across the central or southern Appalachians (Table 1; Figs. 1 and 2). The 62 cases were selected from a larger set of 142 isolated supercells identified and manually tracked across the region from initiation to either

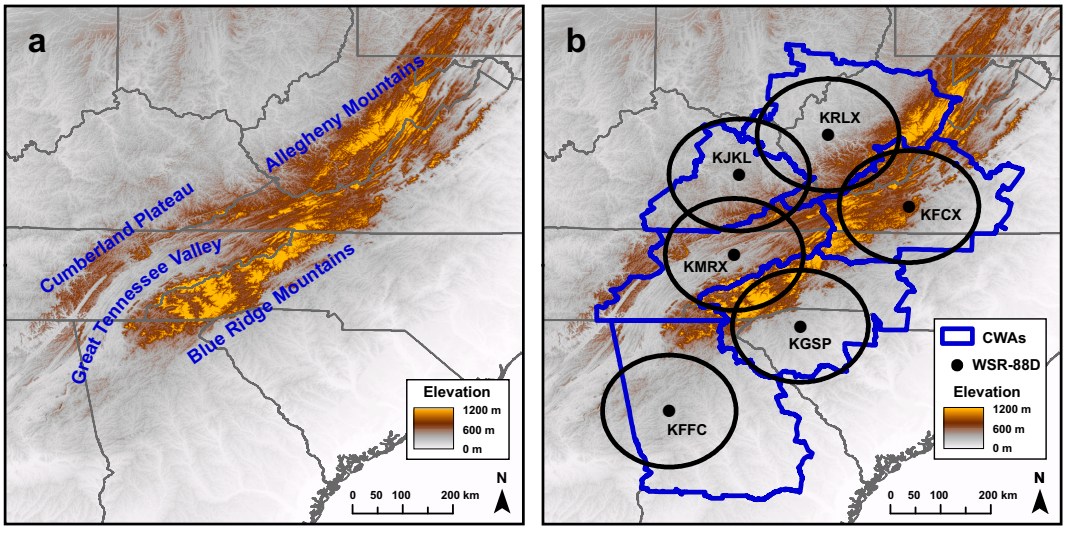

FIG. 1. Surface elevations across the central and southern Appalachians, including the (a) prominent terrain features and (b) county warning areas (CWAs) relevant for all supercells analyzed in the study. The locations of the associated WSR-88D radars and their respective 60 n mi (or 111 km) range rings are denoted in (b) with black circles.

dissipation, merger, or transition to a linear multicell using GR2Analyst software and WSR-88D Level-II data obtained from the NCEI data archive. For a supercell to be considered isolated, the storm had to be approximately one storm width (based on the 35-dBZ echo) away from any other convection (e.g., Bunkers et al. 2006; Gropp and Davenport 2018). Common characteristics among the 62 supercells include the following. First, each storm exhibited either a distinct hook echo or low-level mesocyclone in the radar reflectivity, base velocity (maximum inbound–outbound difference > 15 m s^{-1}), or normalized rotation (>0.1) fields with no evidence of beam blockage for at least five consecutive radar volumes ($\sim$25 min) as the storm passed within 60 n mi (1 n mi = 1.952 km) of a radar. Second, each supercell formed upstream of a prominent terrain feature (either the Cumberland Plateau, Allegheny Mountains, or the Blue Ridge Mountains; Fig. 1) and passed over terrain greater than 400 m in elevation at some point during its lifetime. Third, each supercell exhibited a total lifetime of at least 2 h as an isolated storm (during which continuous supercellular structure was required for only 25 min). Additional details about database development can be found in Purpura et al. (2023).

b. *Supercell categories*

Following Purpura et al. (2023), each supercell was categorized as either "crossing" or "noncrossing" based on the persistence of its supercellular characteristics after interaction with prominent terrain features, which were defined by a 30-m digital elevation model obtained from the USGS data archive. A crossing supercell maintained either a distinct low-level mesocyclone or a hook echo as it traversed at least one prominent ridge. In contrast, a noncrossing supercell maintained neither a distinct low-level mesocyclone nor a hook echo as it traversed a

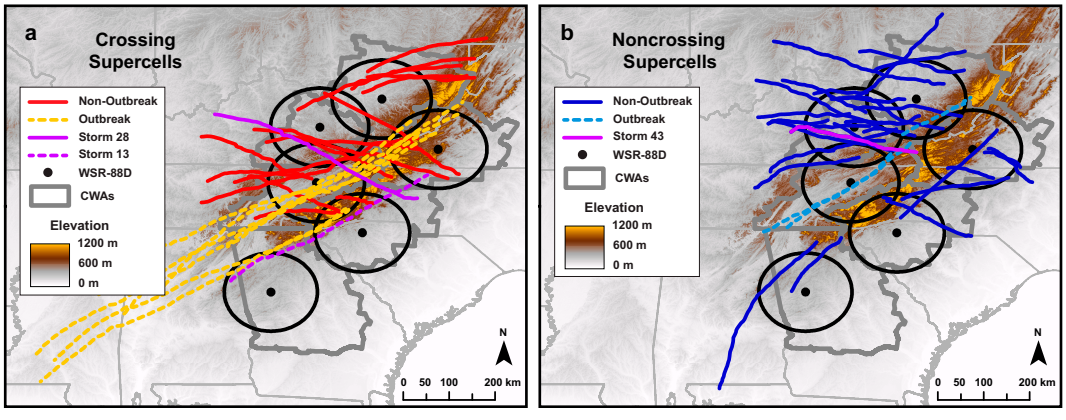

FIG. 2. Tracks for all (a) crossing and (b) noncrossing supercells with the representative example storms (see Figs. 3–5) denoted in purple. The locations of the WSR-88D radars and their respective 60 n mi (or 111 km) range rings are denoted with black circles.

TABLE 2. List of radar-based characteristics evaluated for each radar volume when a supercell was located within the 25–60 n mi annulus from a radar. Characteristic selection and range restriction rationales are provided in the text.

Abbreviation	Radar characteristic description	Units	Methods
DBZMAX	Max base reflectivity	dBZ	Obtained from the 0.5° or 0.9° elevation angle
VILMAX	Max vertically integrated liquid	kg m^{-2}	Based on Stewart (1991)
EETMAX	Max echo top	kft	Based on the highest 10-dBZ echo
MESOINT	Mesocyclone intensity	m s^{-1}	ΔVR between strongest inbound and outbound
MESODEP	Mesocyclone depth	km	Depth over which ΔVR exceeds 15 m s^{-1}
MESODIAM	Mesocyclone diameter	km	Distance between strongest inbound and outbound
NROTMAX	Max normalized rotation	—	Parameter unique to GR2Analyst software
MEHS	Max expected hail size	in.	Based on Witt et al. (1998)
50DBZHGT	Max 50-dBZ echo top	kft	Based on the highest 50-dBZ echo
STMTOPDIV	Storm top divergence	m s^{-1}	ΔVR at echo top elevation
HOOK	Hook echo?	—	Subjectively determined (yes/no)
BWER	Bounded weak echo region?	—	Subjectively determined (yes/no)
STMSPD	Storm speed	m s^{-1}	Obtained from storm center fixes between radar volumes

prominent ridge (i.e., the supercell dissipated or grew upscale). Additional details about this categorization can be found in Purpura et al. (2023). A total of 25 crossing and 37 noncrossing supercells were quasi-objectively identified (Table 1; Fig. 2).

A second categorization, defined as either "outbreak" or "nonoutbreak," was required since ~20% of our cases were associated with the 27–28 April 2011 outbreak involving multiple long-lived tornadic supercells that moved into the southern Appalachians after developing in central Mississippi and Alabama (Table 1; Fig. 2; Gaffin 2012; Knupp et al. 2014). Given that aspects of the mesoscale environment were highly favorable for supercell maintenance during the outbreak, one might expect the outbreak supercells to skew a multicase statistical analyses of radar-based storm structure and intensity. As shown in section 3b, inclusion of the outbreak supercells does skew some results, but it does not markedly alter our overall results.

c. Radar characteristics

The evolution of storm structure and intensity was analyzed using all available WSR-88D radar volumes as each supercell passed through the 25–60 n mi annulus surrounding any of the six radars located in our Appalachian study area (Fig. 1). The outer 60 n mi threshold was used to ensure low-level (below ~2 km) mesocyclone structure was resolvable with sufficient angular resolution, while the inner 25 n mi threshold was used to ensure upper-level storm structure was resolvable beyond the cone of silence. While these range criteria limited our ability to document structural evolution through the full lifetime of each supercell, including when a few storms passed over the highest elevations, the criteria were required to minimize range bias in the analysis. Nevertheless, as shown in section 3, the use of a large multicase database permits insight into typical supercell evolution during their passage through regions with elevated terrain and over prominent terrain features.

For each radar volume, a total of 13 radar-based characteristics were determined to document supercell structure and intensity (Table 2); these characteristics were selected based on prior severe storm research and discussions with collaborating National Weather Service (NWS) offices in the study area to ensure operational applicability. Estimates of updraft intensity and storm depth were quantified using the maxima of base reflectivity, vertically integrated liquid, expected hail size, 50-dBZ echo top, 10-dBZ echo top, and storm top divergence, as their magnitudes and variability have been linked to severe winds (Wakimoto and Bringi 1988; Stewart 1991; Rinehart and Borho 1993) and large hail (Amburn and Wolf 1997; Witt et al. 1998; Murillo and Homeyer 2019). Estimates of mesocyclone intensity, diameter, and depth were quantified from dealiased Doppler radial velocity (VR) data and the maximum normalized rotation provided by the GR2Analyst software (see Table 2), as these parameters have been linked to supercell intensity and tornado production (Trapp et al. 2005; Bosart et al. 2006; Homeyer et al. 2020; Sessa and Trapp 2020). Also, the presence of a hook echo or bounded weak echo region was determined through qualitative examination of the radar reflectivity. Finally, storm speed was calculated from sequential storm centers (defined by either any base mesocyclone center or the base radar reflectivity maximum). When a storm passed through two annuli simultaneously, characteristics were analyzed from only the nearest radar. Overall, radar characteristics were determined from over 1800 radar volumes as the 62 supercells made 88 unique passes through the six annuli (Tables 3 and 4; Fig. 2), as multiple storms passed through two or more annuli during different periods of their lifetime.

TABLE 3. Total crossing and noncrossing supercells that passed within 60 n mi of each radar. Note that the crossing and noncrossing totals listed in the bottom row differ from the number of *unique* supercells (Table 1) due to multiple supercells passing within 60 n mi of two or more radars during their lifetime (Fig. 2).

Radar	Crossing	Noncrossing	Total
KRLX	5	13	18
KJKL	4	20	24
KFCX	6	6	12
KMRX	16	5	21
KGSP	6	2	8
KFFC	3	2	5
Total	40	48	88

TABLE 4. Total analyzed radar volumes among crossing and noncrossing supercells that passed through the 25–60 n mi annulus from each radar.

Radar	Crossing	Noncrossing	Total
KRLX	101	252	353
KJKL	78	320	398
KFCX	170	124	294
KMRX	366	83	449
KGSP	155	57	212
KFFC	57	41	98
Total	927	877	1804

d. Environmental parameters and storm reports

The local environment of each supercell was characterized using hourly 13-km Rapid Update Cycle (RUC) and Rapid Refresh (RAP) model analyses following the methods outlined in Purpura et al. (2023). Numerous sounding-based stability and vertical shear parameters were computed at each grid column to provide context for the structural evolution exhibited by the radar parameters along each storm track, including most-unstable CAPE and CIN (MUCAPE and MUCIN; Thompson et al. 2007), SRH in the 0–1-km (SRH01) and 0–3-km (SRH03) layers, and downdraft convective available potential energy (DCAPE; Gilmore and Wicker 1998), along with the supercell composite parameter (SCP; Gropp and Davenport 2018), and the severe hazard environments with reduced buoyancy parameter (SHERBE; Sherburn and Parker 2014). A full list of computed environmental parameters can be found in Purpura et al. (2023).

To estimate whether a given storm was experiencing upslope or downslope flow, the surface winds and terrain elevations from the hourly 13-km RUC and RAP analyses were used to compute the low-level cross-slope flow (CRSSLP) through the region via

$$\text{CRSSLP} = \mathbf{V} \cdot \nabla \mathbf{Z}, \tag{1}$$

where $\mathbf{V}$ is the surface wind vector and $\nabla \mathbf{Z}$ is the horizontal gradient in surface elevation. Then, the near-storm CRSSLP was computed for each radar-determined storm location via simple space–time interpolation. However, to reduce convective contamination from storm-generated outflows and cold pools, CRSSLPs were computed from the surface winds valid one hour prior to storm passage over a given location. Moreover, it should be noted that the CRSSLP flow represents an *estimate* of the local upslope or downslope flow based on the relatively coarse RUC and RAP terrain; subgrid-scale terrain features will undoubtedly modify the flow (e.g., Katona et al. 2016; Katona and Markowski 2021; Purpura et al. 2023).

Last, to provide context of how storm passage over elevated terrain influenced severe weather production, all local storm reports (tornado, large hail, and severe straight-line winds) associated with the 62 supercells were collected from the SPC event summaries archive and attributed to individual storms by cross referencing the time and location of each report with each storm track. While there are well-documented issues with severe reports (e.g., Doswell and Burgess 1988; Trapp et al. 2006; Edwards et al. 2018), including a potential low bias in rural areas (Anderson et al. 2007; Allen et al. 2015), the available reports indicate that our storms represent a spectrum of tornadic, nontornadic severe, and nonsevere supercells that encountered prominent terrain and produced severe weather as they moved through the study area. Purpura et al. (2023) provides additional details about the storm reports, including summary statistics and environmental context among the crossing and noncrossing cases. Future work may wish to include an analysis of lightning activity as an additional correlation between storm characteristics and hazards (e.g., Schultz et al. 2015), since it does not have the spatial limitations of storm reports.

e. Limitations

We acknowledge that our data and methods contain limitations. While we attempt to make direct connections between trends in supercell characteristics and the underlying terrain, there are temporal and spatial limits to the data, as well as several confounding factors that prevent clean determinations. For example, radar volumes are available every 5–6 min, while RUC/RAP analyses are available hourly, and storm reports can have their own temporal idiosyncrasies for a variety of nonmeteorological reasons. Such differing temporal resolutions can be problematic, as the exact time scale of storm response to various physical, environmental, or other external factors is unknown. Likewise, the 13-km RUC/RAP analyses cannot resolve any near-storm environmental variability induced by finer-scale terrain features. As highlighted in Purpura et al. (2023) and other studies (e.g., Schneider 2009; Markowski and Dotzek 2011; Smith et al. 2016; Gropp and Davenport 2018; Wunsch and French 2020; Brown et al. 2021; Davenport 2021; Flournoy et al. 2021), supercell evolution and severe weather production are governed by a combination of environmental inflow characteristics, internal storm dynamics, and physical terrain effects. Thus, in our subsequent discussion of results, we emphasize overall trends in radar characteristics as they relate to the nearby terrain, but we also identify multiple additional factors that could be contributing.

3. Results

a. Representative supercell cases

Despite differences in synoptic patterns, local environments (instability and vertical shear), life stage (developing, mature, or dissipating), and local terrain, many similarities in structure and evolution were observed as the supercells passed through the 25–60 n mi annulus of a radar. Here, we present time series of radar characteristics, cross-slope flow, and storm reports for three representative mature supercells. The first (Storm 28; Fig. 3) exemplifies crossing storms that traverse terrain at a more orthogonal angle to the main ridgelines (Figs. 1 and 2). The second (Storm 13; Fig. 4) exemplifies crossing storms that traverse secondary ridges while moving

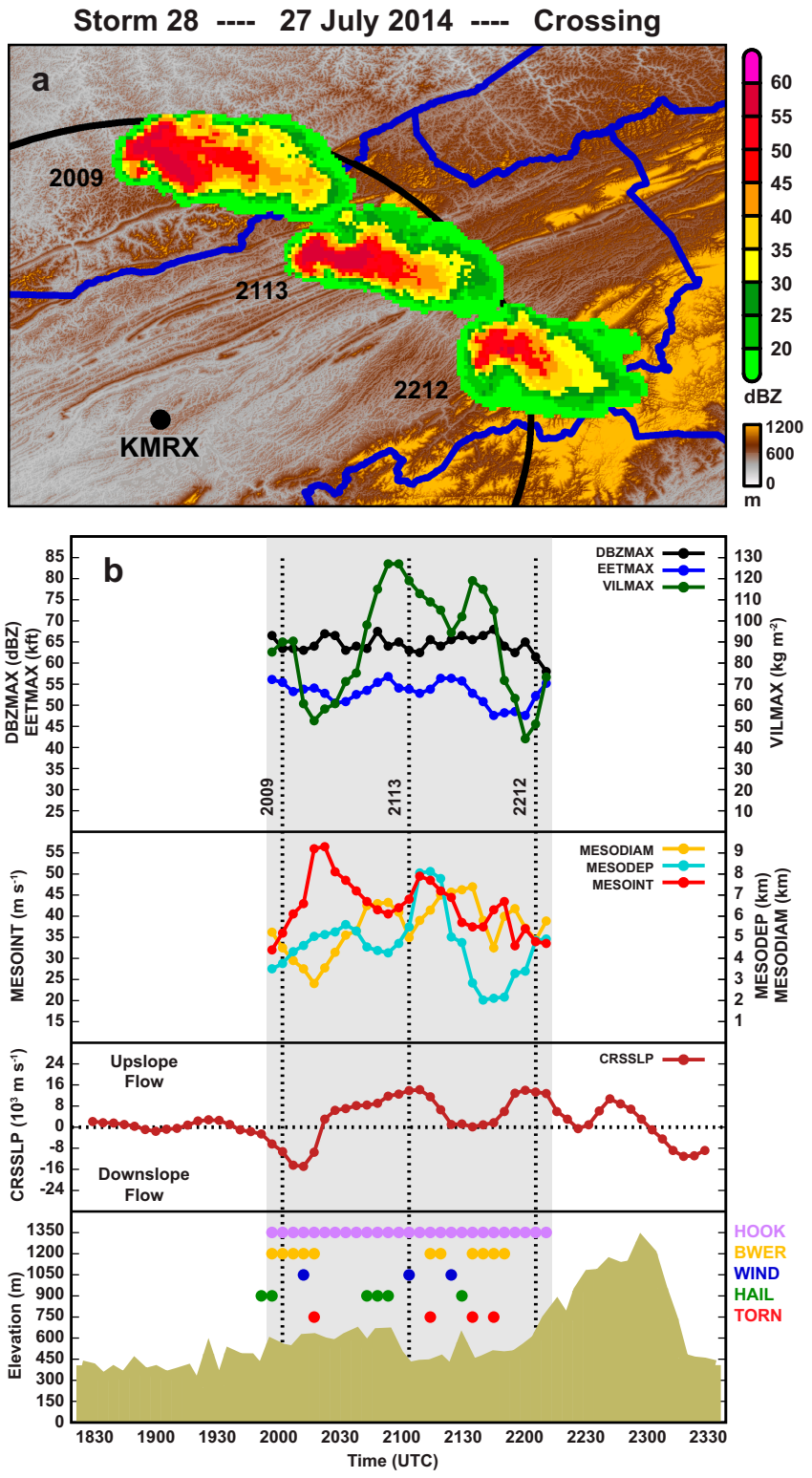

FIG. 3. (a) Base-level radar reflectivity at select times on 27 Jul 2014 as Storm 28 crossed the Cumberland Plateau and passed within 60 n mi (black range ring) of KMRX. Blue lines denote CWA boundaries, and the local terrain is shown. (b) Time series of select radar-based characteristics (top two panels) as the storm passed through the 25–60 n mi annulus of the

more parallel to the main ridgelines. The third (Storm 43; Fig. 5) exemplifies noncrossing storms that either dissipate or transition to a multicell as they interact with elevated terrain.

1) STORM 28—CROSSING

Storm 28 developed around 1600 UTC 27 July 2014 in central Kentucky [300 km northwest of Morristown, Tennessee (KMRX)] ahead of an eastward-moving cold front. The local environment was supportive of supercell formation (MUCAPE $\approx$ 2500 J kg^{-1}; SRH03 $\approx$ 200 m^2 s^{-2}; SCP $\approx$ 13), and supercellular structure (a hook echo and low-level mesocyclone) was evident by 1830 UTC (not shown). The storm moved southeast, approaching the Appalachians at an angle nearly orthogonal to the primary ridgelines (see Fig. 2a).

Around 2000 UTC, the now mature supercell moved within 60 n mi of KMRX and began ascending onto the Cumberland Plateau (Fig. 3). During the ascent, Storm 28 exhibited enhanced VILMAX and several hail reports. Over the next 30 min, as the storm crossed the plateau through an environment characterized by low-level downslope flow, less instability (MUCAPE $\approx$ 1000 J kg^{-1}), but more low-level helicity (SRH03 $\approx$ 250 m^2 s^{-2}), a more prominent hook echo developed, the MESOINT and MESODEP increased, the MESODIAM decreased, and one tornado was reported. Such evolution also coincided with a prominent decrease in VILMAX and several wind reports, suggesting a rear-flank downdraft surge was potentially responsible for tornadogenesis (e.g., Markowski 2002). Around 2030 UTC, as the storm approached the plateau edge, the low-level flow became upslope, and both EETMAX and VILMAX increased in conjunction with several hail reports, consistent with a terrain-enhanced updraft (Markowski and Dotzek 2011; Smith et al. 2016). Soon after 2100 UTC, as the storm descended into the Great Tennessee Valley, the MESOINT and MESODEP increased, the MESODIAM decreased, and a second tornado was reported. The catalyst for this tornado may have been a combination of leeside vortex stretching along with local enhancements in instability and low-level helicity (MUCAPE $\approx$ 2000 J kg^{-1}; SRH03 $\approx$ 350 m^2 s^{-2}) due to the channeling of warm moist air up the valley from the southwest (e.g., Bosart et al. 2006; Schneider 2009; Tang et al. 2016). Over the next 60 min, as the storm crossed the valley, maxima in EETMAX (at ~2115 UTC), VILMAX (~2130 UTC), DBZMAX (~2145 UTC), and MESOINT (~2145 UTC) were observed, along with additional wind, hail, and tornado reports.

At 2215 UTC, Storm 28 moved beyond 60 n mi of KMRX while ascending into the Blue Ridge Mountains. The higher intramountain environment contained marginal instability (MUCAPE $\approx$ 800 J kg^{-1}) but moderate low-level helicity (SRH03 $\approx$ 250 m^2 s^{-2}), supporting the weak supercell while crossing the terrain (not shown), before dissipating around 2330 UTC in the more stable (MUCAPE $\approx$ 700 J kg^{-1}; MUCIN ≈ -150 J kg^{-1}) leeward environment.

2) STORM 13—CROSSING

Storm 13 developed around 0200 UTC 28 April 2011 in east-central Alabama [350 km southwest of Greer, South Carolina (KGSP)] ahead of a strong eastward-moving cold front; this storm was one of the supercells from the 27–28 April 2011 outbreak (Knupp et al. 2014). The local environment was extremely favorable for supercell formation (MUCAPE $\approx$ 2200 J kg^{-1}; SRH03 $\approx$ 500 m^2 s^{-2}; SCP $\approx$ 23), and a low-level mesocyclone was first detected around 0300 UTC by the Peachtree City, Georgia (KFFC), radar (not shown). The storm moved rapidly northeast, approaching the Blue Ridge Mountains at an angle nearly parallel to the primary ridgelines (see Fig. 2a).

Around 0445 UTC, the mature supercell moved within 60 n mi of KGSP as it began interacting with some southern foothills (Fig. 4). The intramountain environment was supportive of supercells (SCP $\approx$ 5) and severe weather production (SHERBE $\approx$ 1.5) through a combination of marginal instability (MUCAPE $\approx$ 600 J kg^{-1}) and large low-level helicity (SRH03 $\approx$ 500 m^2 s^{-2}). Over the next two hours, the supercell crossed several secondary ridges with local elevation changes of 200–500 m. During at least two ascents (around 0530 and 0615 UTC), the low-level flow was upslope, and the storm exhibited increasing VILMAX, DBZMAX, and/or EETMAX along with distinct BWER, consistent with a terrain-enhanced updraft. Despite these apparent updraft amplifications, large hail and severe wind reports were scarce; likely due to a combination of the limited updraft instability, minimal downdraft instability (DCAPE $\approx$ 300 J kg^{-1}), and a low population density through the area. During at least two descents (around 0515 and 0630 UTC), the low-level flow was downslope, and the supercell exhibited increasing MESOINT and MESODEP along with decreasing MESODIAM (Fig. 4d), consistent with leeside stretching of the mesocyclone. Notably, a tornado report coincided with the 0515 UTC descent.

Just after 0700 UTC, Storm 13 moved beyond 60 n mi of KGSP and began traversing the relatively flat Piedmont region leeward of the Blue Ridge Mountains. As the storm continued northeast, the local environment became increasingly more stable (MUCAPE $<$ 300 J kg^{-1}; MUCIN < -60 J kg^{-1}) and less favorable for supercells (SCP $<$ 0.5), leading to storm dissipation around 0830 UTC.

←

radar (gray shading), along with the cross-slope flow (third panel), the local terrain elevation (brown; bottom panel) beneath the storm, and times when the storm exhibited and/or produced a hook echo (purple circles), a bounded weak echo region (gold circles), severe winds (blue circles), large hail (green circles), or a tornado (red circles). Vertical dashed lines in (b) denote times with corresponding radar observations shown in (a). The storm track is shown in Fig. 2a. See Table 2 for radar characteristic definitions and section 2d for the cross-slope flow definition.

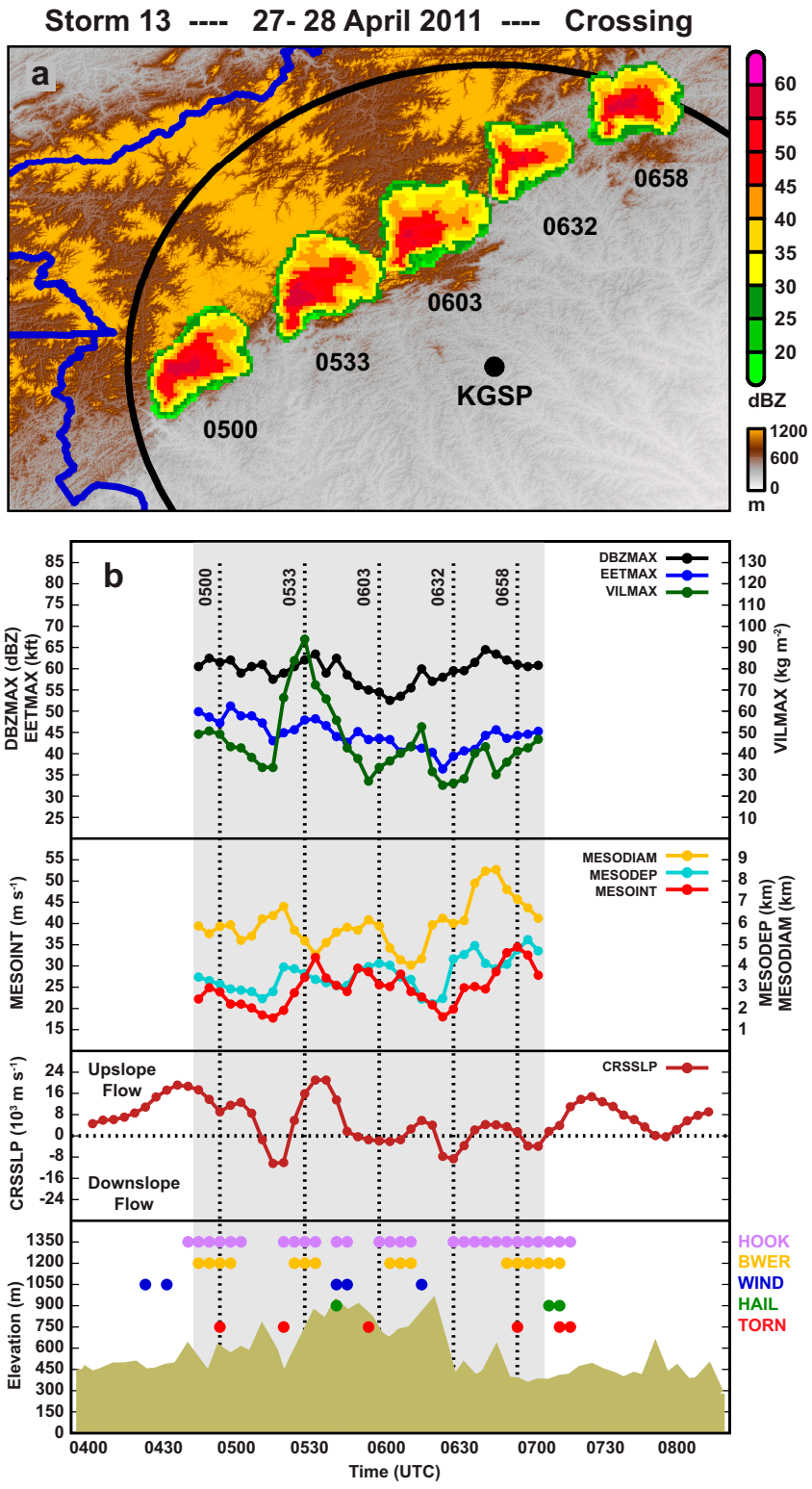

FIG. 4. As in Fig. 3, but for select times on 28 Apr 2011 as Storm 13 crossed the Blue Ridge Mountains and passed within 60 n mi (black range ring) of KGSP. The storm track is shown in Fig. 2a. See Table 2 for radar characteristic definitions and section 2d for the cross-slope flow definition.

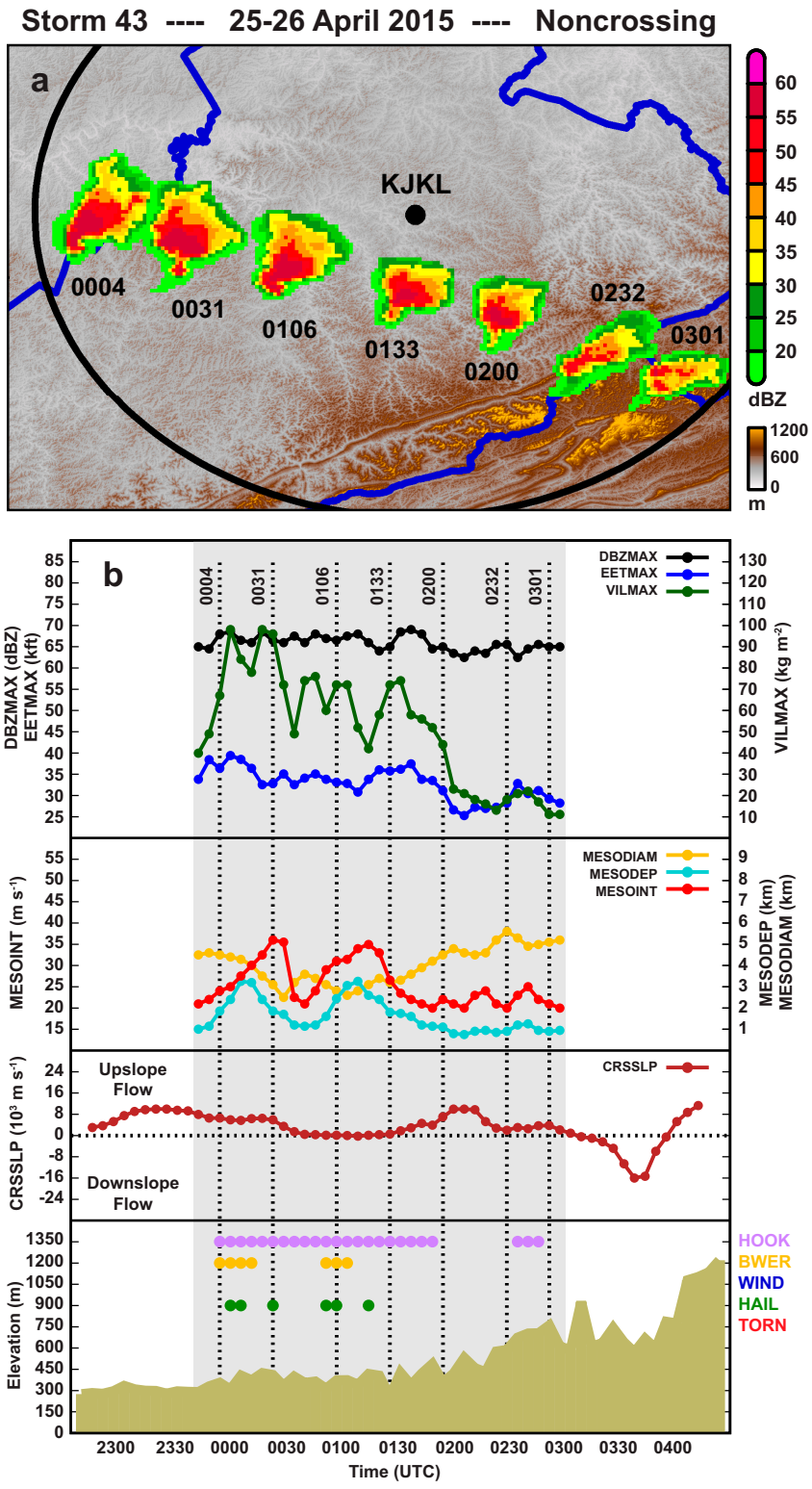

FIG. 5. As in Fig. 3, but for select times on 25–26 Apr 2015 as Storm 43 crossed the Allegheny Mountains and passed within 60 n mi (black range ring) of KJKL. The storm track is shown in Fig. 2b. See Table 2 for radar characteristic definitions and section 2d for the cross-slope flow definition.

3) STORM 43—NONCROSSING

Storm 43 developed around 2245 UTC 25 April 2015 in central Kentucky [150 km west of Jackson, Kentucky (KJKL)] just south of an east–west stationary front. The local environment was marginally supportive of supercells (SCP ≈ 3) with sufficient instability (MUCAPE ≈ 650 J kg^{-1}) and large low-level helicity (SRH03 ≈ 350 m^2 s^{-2}). The storm moved east slowly (Fig. 2b) and began exhibiting a hook echo and a low-level mesocyclone around 2345 UTC (not shown).

Around 0000 UTC 26 April, the now mature supercell moved within 60 n mi of KJKL as it began interacting with the western foothills of the Alleghany Mountains (Fig. 5). Over the next two hours, the storm exhibited several updraft surges (denoted by peaks in VILMAX) and multiple large hail reports as it crossed terrain that varied by 50–200 m. Two prominent surges coincided with increased MESOINT and MESODEP, but the mesocyclone remained smaller than those in Storm 13 or Storm 28 (see Figs. 3b and 4b) and no tornadoes were reported. Notably, the modest terrain induced few modifications to the low-level vertical shear, helicity, or instability. Around 0200 UTC, despite an increase in upslope flow, the VILMAX, EETMAX, and MESOINT decreased dramatically as the storm moved into higher elevations (>500 m) and a local environment less supportive of supercells (SCP ≈ 1; MUCAPE ≈ 500 J kg^{-1}; SRH03 ≈ 275 m^2 s^{-2}) and severe weather production (SHERBE ≈ 1.0). Such collective evolution reinforces the notion that internal storm dynamics and environmental changes can outweigh any terrain-induced factors, such as upslope, that may be favorable for supercell intensification.

By 0330 UTC, Storm 43 had moved beyond 60 n mi of KJKL and began traversing the higher elevations of the Alleghany Mountains. As the storm continued moving east-southeast at an angle nearly orthogonal to the primary ridgelines, the local low-level flow transitioned to downslope and the environment became increasingly more stable (MUCAPE < 300 J kg^{-1}) and less favorable for supercells (SCP < 0.4), leading to storm dissipation around 0430 UTC.

b. *Comparison of crossing and noncrossing supercells*

The representative cases described above highlight several differences between crossing and noncrossing supercells. Notably, crossing storms often exhibited larger and more intense mesocyclones, and, at times, greater storm depth and more intense updrafts. To elucidate whether such differences can aid short-term forecasting, we now quantify radar characteristic differences between crossing and noncrossing supercells. Given the intra-annulus variability of each storm (Figs. 3–5), and larger sample sizes (Table 4), we use sample distributions constructed from radar volumes (rather than from unique supercell passes; Table 3) but focus only on differences whereby a two-tailed t test adjusted for serial autocorrelation (Wilks 2006) exhibited significance at the $p < 0.05$ (or 95% confidence) level between the respective distribution means. Analyses were conducted using the full database, along with stratifications by radar (or county warning area) and outbreak category. Overall, differences among individual radars were largely consistent with those of the full database (see McKeown 2021), so only results for the full database with the outbreak stratification are discussed.

Figures 6–8 show the paired distributions (crossing versus noncrossing) of radar characteristics for all supercells, as well as the outbreak and nonoutbreak cases. Table 5 lists the corresponding distribution means and p values for their differences. Notably, the updraft intensity and storm depth metrics (Fig. 6) exhibited no statistically significant differences among all supercells or the nonoutbreak cases. Given that updraft intensity is closely related to local instability, such results are consistent with the lack of significant differences found among most near-storm environmental stability parameters evaluated by Purpura et al. (2023) for the same cases. In contrast, among the outbreak cases, the crossing storms exhibited significantly greater EETMAX, 50DBZHGT, and STMTOPDIV, indicative of deeper and more intense updrafts.

The most significant differences between crossing and noncrossing supercells were among mesocyclone characteristics (Fig. 7). Specifically, crossing storms exhibited greater MESOINT (by ~8–12 m s^{-1}), MESODEP (~1–2 km), MESODIAM (~1–2 km), and NROTMAX (~0.25) for all stratifications (Table 5). Given that mesocyclone characteristics are closely linked to low-level vertical shear and helicity, such results are consistent with the significantly larger near-storm environmental shear and helicity found by Purpura et al. (2023) for crossing cases in the higher-elevation intramountain regions. Moreover, the crossing cases exhibited greater spread within each distribution, which may reflect their prolonged interaction with terrain, including terrain-induced environmental variability (e.g., Katona et al. 2016) and structural evolution (e.g., Markowski and Dotzek 2011; Smith et al. 2016). This topic is explored further in section 3c using a subset of crossing supercells that passed over prominent terrain features.

Differences in BWER and HOOK frequencies among crossing and noncrossing storms were also apparent. Specifically, crossing supercells exhibited a HOOK in ~54% of all radar volumes, whereas noncrossing storms exhibited a HOOK in ~33% of radar volumes. Likewise, BWERs were identified in ~32% of radar volumes for crossing storms, but only ~14% of volumes for noncrossing storms. Such qualitative differences support the notion that crossing supercells often contain stronger mesocyclones, and occasionally stronger updrafts, than the noncrossing storms that pass through the southern and central Appalachian region.

Last, there were significant differences in storm speed between crossing and noncrossing supercells (Fig. 8). Among all supercells and the nonoutbreak cases, crossing storms moved faster (by ~5 m s^{-1}) than noncrossing storms. Such differences are consistent with crossing storms developing in and traversing through synoptic environments more conducive to supercell maintenance (i.e., with strong upper-level winds, a prominent low-level jet, and strong low-level vertical shear; Purpura et al. 2023). Inherently, such environments also exhibit stronger mean wind speeds that lead to faster storm motions. Moreover, the lack of significant differences among the outbreak cases underscores the importance of the synoptic-scale environment on storm speed (i.e., all outbreak supercells developed in a common synoptic environment, and thus, moved at similar speeds).

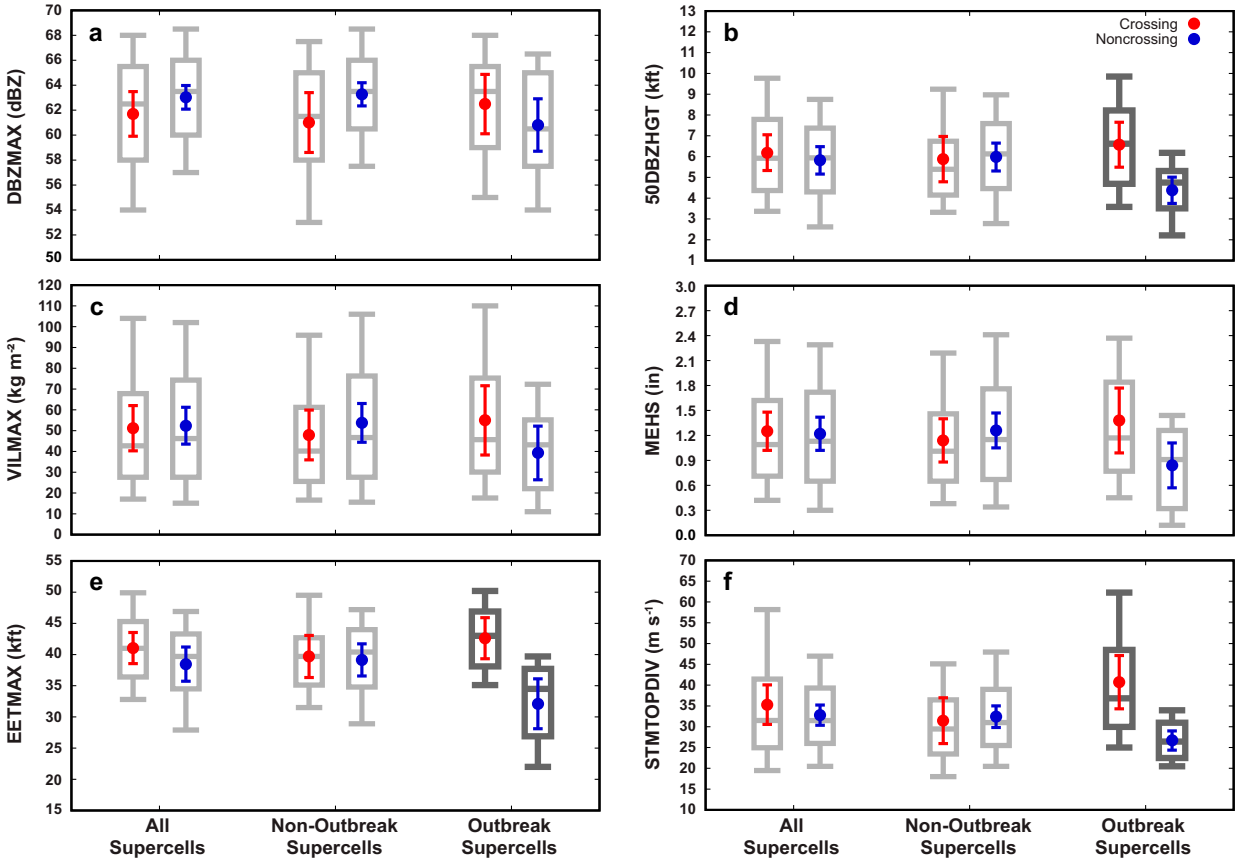

FIG. 6. Statistical summaries of the (a) DBZMAX, (b) 50DBZHGT, (c) VILMAX, (d) MEHS, (e) EETMAX, and (f) STMTOPDIV for crossing (red) and noncrossing (blue) supercells passing through the 25–60 n mi annulus of a radar. Summaries are shown for all supercells (at left), nonoutbreak supercells (at center), and outbreak supercells (at right) in each panel; nonoutbreak supercells exclude the 12 storms observed during the 27–28 Apr 2011 outbreak. For each distribution, the box center and ends denote the median (50%), first quartile (25%), and third quartile (75%), respectively, while the whiskers denote the 10% and 90% values; the means (red and blue circles) and 95% confidence intervals (error bars) are also shown. Box-and-whisker plot pairs shown in dark gray denote distributions statistically different at the 5% level based on a *t* test adjusted for serial autocorrelation. See Table 2 and the text for characteristic definitions and methods.

c. Supercells crossing prominent terrain

Another notable feature among the representative crossing supercells (Figs. 3 and 4) was the frequent modulation of updraft intensity, storm depth, mesocyclone structure, and/or increased severe weather production as storms ascended and/or descended prominent peaks or ridges. To determine whether such storm evolution was common, which could benefit short-term forecasting, we quantified statistical differences among the radar characteristics within a "peak-relative" framework among those storms that traversed prominent peaks/ridges. Our approach was the following. First, all prominent terrain peaks (elevation maximum $>$ 500 m MSL with elevation decreases $>$ 200 m MSL within $\pm$30 km of the maximum) were identified along all crossing supercell tracks; noncrossing storms were not analyzed. Second, to focus on mature supercells (rather than developing or dissipating storms), the identified peaks were restricted to those $>$60 min after initiation and $>$60 min before dissipation or upscale growth. Third, using an 11-radar-volume analysis window centered on the maximum elevation, the identified peaks were further restricted to those with windows fully inside the 25–60 n mi annulus from a radar. Given typical storm speeds (Fig. 8) and radar volume intervals ($\sim$5 min), the 11-volume window corresponds to roughly $\pm$30 km or $\pm$25 min of peak elevation. Last, when overlapping windows were identified, only the window with the highest peak elevation was retained. Overall, such methods identified 35 unique peak-relative analysis windows among the 26 crossing supercells (i.e., two unique windows were identified for nine storms).

Next, statistical summaries of the terrain, cross-slope flow, radar characteristics, and storms reports within this peak-relative framework were created. For the terrain, cross-slope flow, and continuous radar metrics, differences from their respective value at peak elevation were first computed for each volume within all 35 windows, and then the differences were summarized for each peak-relative window location (Fig. 9). For the categorical radar characteristics (HOOK and BWER), the percentage of all 35 peak-relative window locations

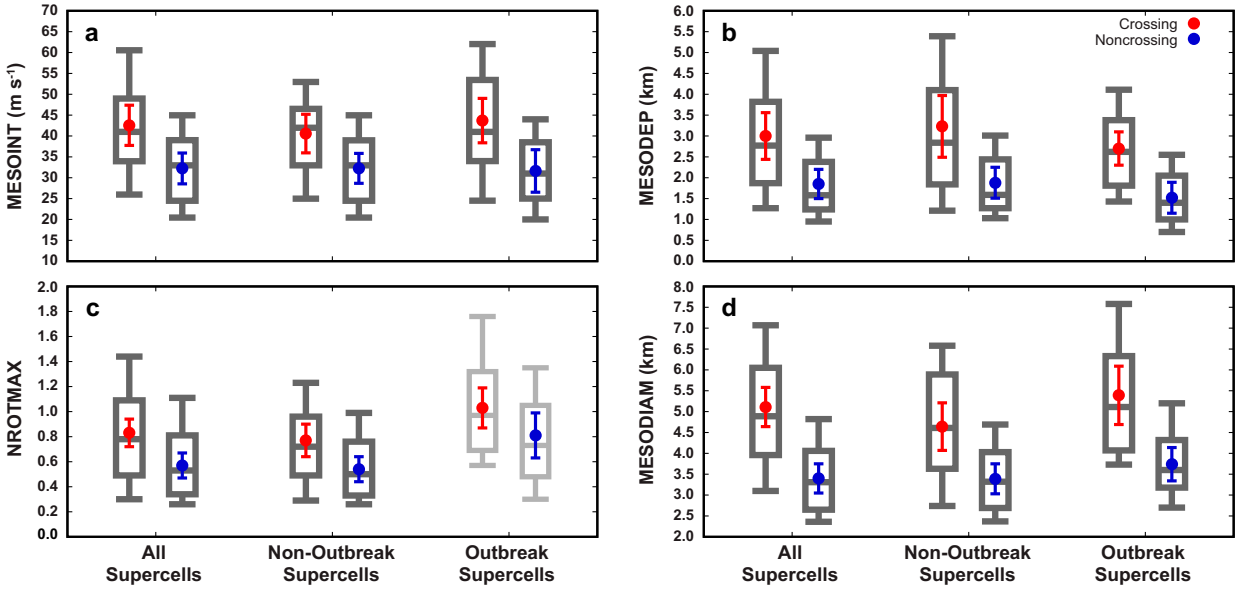

FIG. 7. As in Fig. 6, but for (a) MESOINT, (b) MESODEP, (c) NROTMAX, and (d) MESODIAM. See Table 2 and the text for characteristic definitions and methods.

exhibiting such features were tabulated (Fig. 9b). Last, for the storm reports, all report types were totaled within the peak-relative framework, and then percentages for each type were computed for each peak-relative window location (Fig. 9b). Hence, by focusing on peak-relative differences whereby a two-tailed t test adjusted for serial autocorrelation (Wilks 2006) exhibited significance at the $p < 0.05$ (or 95% confidence) level (i.e., the dark gray box-and-whisker plot in Fig. 9), we can elucidate which radar characteristics exhibit significant change as supercells cross typical prominent peaks and ridges (Fig. 9a), and how such storm evolution translates to severe weather production. While clear connections are somewhat tenuous given the limitations of storm reports (see section 2d), identifying such trends may nevertheless have operational utility.

As the supercells ascended the prominent peaks/ridges, the significantly greater upslope flow (by ~2–5 m s^{-1}; Fig. 9c), DBZMAX (by ~2 dBZ; Fig. 9d), VILMAX (by ~5–10 kg m^{-2}; Fig. 9f), and EETMAX (by ~1 kft; Fig. 9h) observed roughly 10–20 km prior to reaching peak elevation are consistent with terrain-enhanced updrafts (Markowski and Dotzek 2011; Smith et al. 2016). At the same time, the significantly greater MESOINT (by ~5 m s^{-1}; Fig. 9e) and MESODEP (by ~0.6 km; Fig. 9g), combined with a modest reduction in MESODIAM (by ~0.5 km; Fig. 9i), are consistent with mesocyclone intensification via vortex stretching, but may also reflect a lagged response to enhanced instability and storm-relative helicity induced by the channeling of warm moist air up a valley from which the storm ascended (Bosart et al. 2006; Schneider 2009; Tang et al. 2016; Wunsch and French 2020). Notably, local intra-window maxima in large hail and tornado reports (Fig. 9b) coincided with such upslope storm evolution.

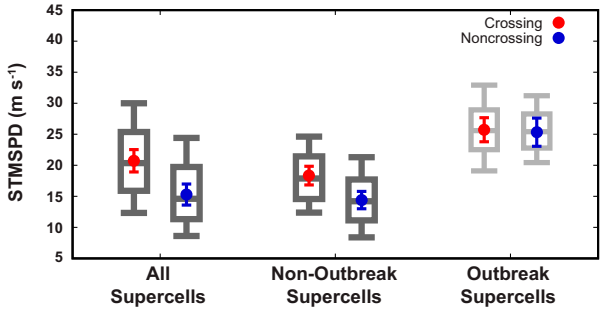

FIG. 8. As in Fig. 6, but for STMSPD. See Table 2 and the text for characteristic definitions and methods.

Subsequently, as the supercells passed over the peak elevation, decreases in DBZMAX (by ~3 dBZ), VILMAX (by ~10 kg m^{-2}), and EETMAX (by ~2 kft), along with HOOK and BWER frequency, were observed within ±10 km of the elevation maximum, suggesting a decrease in updraft intensity combined with a possible increase in downdraft intensity and microburst frequency (e.g., Wakimoto and Bringi 1988; Stewart 1991; Rinehart and Borho 1993). Notably, a local maximum in severe wind reports near the peak elevation (Fig. 9b) is consistent with enhanced downdraft activity, but it may also simply reflect the terrain extending upward into the stronger midlevel flow or a shallower boundary layer (see Purpura et al. 2023).

Finally, as the supercells descended the prominent peaks/ridges, a significant increase in MESODEP (by ~1 km), combined with a modest increase in MESOINT (by 2–3 m s^{-1}), a modest decrease in MESODIAM (by ~0.5 km), and a maximum in tornado frequency, were observed 10–20 km after crossing the peak elevation, indicating that leeside mesocyclone intensification, stretching,

TABLE 5. Radar-based characteristic means among crossing and noncrossing subsets for all supercells (left), nonoutbreak supercells (middle), and outbreak supercells (right), along with their corresponding p value from a t test adjusted for serial autocorrelation. Statistics shown in bold denote mean differences significant at the 5% level. Nonoutbreak supercells exclude the 12 storms observed during the 27–28 Apr 2011 outbreak.

	All supercells			Nonoutbreak supercells			Outbreak supercells		
Characteristic	Crossing	Noncrossing	p value	Crossing	Noncrossing	p value	Crossing	Noncrossing	p value
DBZMAX	61.7	63.0	0.096	61.0	63.3	0.064	62.5	60.8	0.269
VILMAX	51.2	52.4	0.433	47.9	53.8	0.247	54.9	39.3	0.173
EETMAX	41.0	38.5	0.088	39.7	39.1	0.399	**42.6**	**32.1**	**0.006**
MESOINT	**42.6**	**32.2**	**0.023**	**40.6**	**32.3**	**0.024**	**43.7**	**31.6**	**0.021**
MESODEP	**3.00**	**1.85**	**0.001**	**3.23**	**1.88**	**0.004**	**2.70**	**1.52**	**0.001**
MESODIAM	**5.10**	**3.40**	**0.000**	**4.64**	**3.38**	**0.001**	**5.39**	**3.74**	**0.000**
NROTMAX	**0.83**	**0.57**	**0.006**	**0.77**	**0.54**	**0.025**	1.03	0.81	0.123
MEHS	1.25	1.22	0.419	1.14	1.26	0.244	1.38	0.84	0.063
50DBZHGT	6.2	5.8	0.247	5.9	6.0	0.444	**6.6**	**4.4**	**0.025**
STMTOPDIV	35.3	32.8	0.197	31.5	32.4	0.225	**40.7**	**26.7**	**0.001**
STMSPD	**20.7**	**15.3**	**0.000**	**18.3**	**14.4**	**0.003**	25.7	25.3	0.308

and contraction was more common than not. However, the mechanisms responsible for such evolution remain unclear. Evidence of leeside updraft intensification was limited; the DBZMAX, VILMAX, and EETMAX often decreased or remained unchanged, and low-level flow was often downslope. Careful examination of those cases with a leeside MESODEP increase (21 of the 35 cases) revealed that 12 cases (or ~57%) may have been aided by the channeling of warm moist air through the leeside valley (Fig. 3; Bosart et al. 2006; Schneider 2009; Tang et al. 2016). Other possible contributing mechanisms include cold pool interactions with the terrain (Mulholland et al. 2019), terrain-induced gravity waves (Lyza et al. 2020), and local variations in surface roughness (Houser et al. 2020).

4. Summary

This study examined radar characteristics of 62 isolated supercells that occurred within the central and southern Appalachian Mountains (Figs. 1 and 2), extending the environmental analysis conducted by Purpura et al. (2023) on the same supercells. Our overall goal was to improve short-term forecasts of supercells traversing the region's complex terrain. The supercells were categorized as either crossing (~40%; storms that maintained supercellular structure during terrain interactions) or noncrossing (~60%; storms that dissipated or grew upscale upon terrain interaction); significant differences between the two categories are summarized below within the context of multiple radar-based characteristics (Table 2) and severe storm reports.

The primary structural discriminator between crossing and noncrossing supercells was their mesocyclone; crossing storms had significantly stronger, wider, and deeper mesocyclones (Table 5; Fig. 7), along with more prominent and persistent low-level hook echoes. Crossing storms also moved faster (Fig. 8). However, significant differences in radar-based characteristics indicative of updraft intensity and storm depth were negligible (Fig. 6). Overall, such results are consistent with the environmental analysis by Purpura et al. (2023), which identified low-level shear and storm-relative helicity (i.e., parameters physically related to mesocyclone variability; Davies-Jones 1984; Rotunno and Klemp 1985) as the best discriminators between crossing and noncrossing storms.

Further examination of those supercells that crossed prominent peaks and ridges revealed significant increases in maximum reflectivity, vertically integrated liquid, echo tops, and mesocyclone intensity/depth, along with local maxima in large hail and tornado reports, as storms ascended windward slopes (Fig. 9). Then, as storms descended leeward slopes, significant increases in mesocyclone depth and tornado frequency were observed, coupled with a modest increase in mesocyclone intensity and small decreases in mesocyclone width, radar reflectivity, vertically integrated liquid, and echo tops. Overall, such results are consistent with the notions that terrain-enhanced updrafts are common on windward slopes (Markowski and Dotzek 2011; Smith et al. 2016), while mesocyclone stretching, intensification, and contraction are common on leeward slopes (Prociv 2012).

While this study contributes to a better understanding of supercell–terrain interactions, several questions remain open for additional research. For example, how representative are the results for other regions with complex terrain? How do variations in low-level flow relative to fine-scale terrain, combined with variations in the storm's approach angle to the terrain, influence storm evolution? How does variability in the leeside terrain (e.g., slope and valley orientation) relative to the prevailing low-level flow modulate leeside mesocyclone evolution? Do crossing and noncrossing supercells exhibit significant differences and/or trends in dual-polarimetric radar characteristics while traversing prominent terrain? Such questions are best addressed through additional case studies, larger multistorm analyses, and numerical simulations. Our ongoing work involves multiple high-resolution simulations of supercells developing within various observed environments, approaching idealized ridges and realistic terrain from various approach angles and low-level

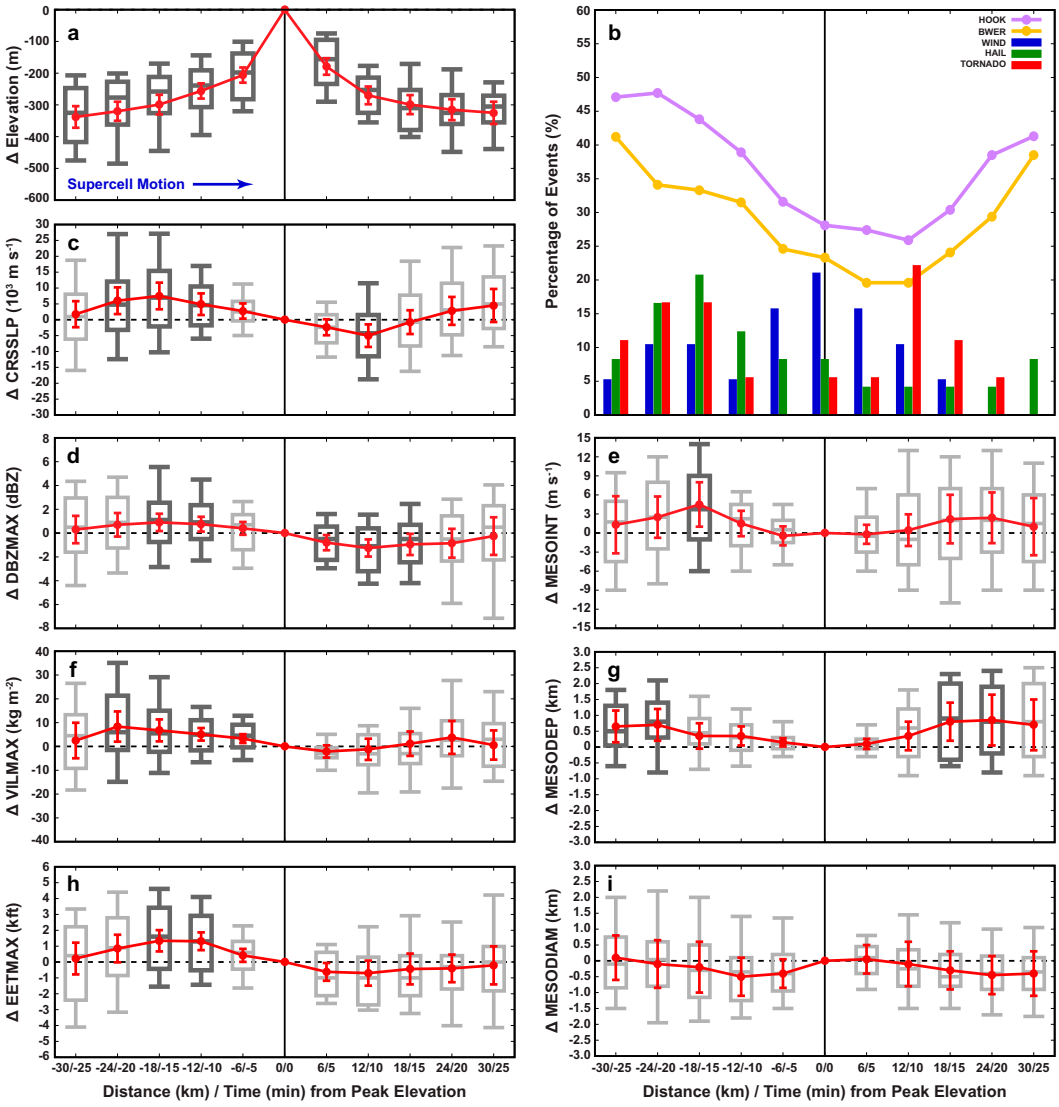

FIG. 9. Summary statistics of (a) surface elevation, (b) severe reports and supercell structure, (c) CRSSLP, (d) DBZMAX, (e) MESOINT, (f) VILMAX, (g) MESODEP, (h) EETMAX, and (i) MESODIAM within an 11-radar-volume peak-relative analysis window centered on the peak elevation (i.e., ±5 radar volumes from the peak) for the 35 cases when a supercell crossed a prominent peak or ridge. Supercell motion was from left to right. Characteristics summarized via box-and-whisker plot distributions are shown as differences from their respective peak-elevation value. For each distribution, the box center and ends denote the median (50%), first quartile (25%), and third quartile (75%), respectively, while the whiskers denote the 10% and 90% values; the means (red circles) and 95% confidence intervals (error bars) are also shown. Distributions shown in dark gray denote means statistically different from the nearby peak-elevation value at the 5% level based on a *t* test adjusted for first-order autocorrelation. Statistics shown in (b) include the percentage of supercells exhibiting a HOOK echo (purple), BWER (orange), or producing severe winds (blue), large hail (green), or a tornado (red) as a function of radar volume relative to the peak elevation. See Table 2 and the text for definitions and methods.

flow scenarios, and experiencing initial interactions with prominent terrain at different life stages.

Acknowledgments. This project was funded by the NOAA Collaborative Science Technology and Applied Research (CSTAR) Program Award Grant NA19NWS4680003. The authors are deeply grateful for the invaluable suggestions and feedback provided throughout this study by the Storm Prediction Center and the National Weather Service Offices at Peachtree City, Georgia; Greenville–Spartanburg, South Carolina; Jackson, Kentucky; Charleston, West Virginia; Blacksburg, Virginia; and Morristown, Tennessee. Constructive comments by three reviewers further clarified our methods and results.

Data availability statement. All data sources used herein are available online. WSR-88D Level-II data were obtained through the NCEI archive at https://www.ncdc.noaa.gov/nexradinv/. Surface elevation data were obtained from the USGS archive at https://www.usgs.gov/products/data/. RUC and RAP model analyses were accessed through https://www.ncei.noaa.gov/products/weather-climate-models/rapid-refresh-update/. Severe storm reports were obtained from the SPC archive at https://www.spc.noaa.gov/climo/online/. Time series of all radar parameters for each supercell case, along with project-specific C++ analysis software, are available upon request.

REFERENCES

Allen, J. T., M. K. Tipett, and A. H. Sobel, 2015: An empirical model relating U.S. monthly hail occurrence to large-scale meteorological environment. *J. Adv. Model. Earth Syst.*, **7**, 226–243, https://doi.org/10.1002/2014MS000397.

Amburn, S. A., and P. L. Wolf, 1997: VIL density as a hail indicator. *Wea. Forecasting*, **12**, 473–478, https://doi.org/10.1175/1520-0434(1997)012<0473:VDAAHI>2.0.CO;2.

Anderson, C. J., C. K. Wikle, Q. Zhou, and J. A. Royle, 2007: Population influences on tornado reports in the United States. *Wea. Forecasting*, **22**, 571–579, https://doi.org/10.1175/WAF997.1.

Bosart, L. F., A. Seimon, K. D. LaPenta, and M. J. Dickinson, 2006: Supercell tornadogenesis over complex terrain: The Great Barrington, Massachusetts, tornado on 29 May 1995. *Wea. Forecasting*, **21**, 897–922, https://doi.org/10.1175/WAF957.1.

Brown, M. C., C. J. Nowotarski, A. R. Dean, B. T. Smith, R. L. Thompson, and J. M. Peters, 2021: The early evening transition in southeastern U.S. tornado environments. *Wea. Forecasting*, **36**, 1431–1452, https://doi.org/10.1175/WAF-D-20-0191.1.

Bunkers, M. J., M. R. Hjelmfelt, and P. L. Smith, 2006: An observational examination of long-lived supercells. Part I: Characteristics, evolution, and demise. *Wea. Forecasting*, **21**, 673–688, https://doi.org/10.1175/WAF949.1.

Davenport, C. E., 2021: Environmental evolution of long-lived supercell thunderstorms in the Great Plains. *Wea. Forecasting*, **36**, 2187–2209, https://doi.org/10.1175/WAF-D-21-0042.1.

Davies-Jones, R., 1984: Streamwise vorticity: The origin of updraft rotation in supercell storms. *J. Atmos. Sci.*, **41**, 2991–3006, https://doi.org/10.1175/1520-0469(1984)041<2991:SVTOOU>2.0.CO;2.

Doswell, C. A., III, and D. W. Burgess, 1988: On some issues of United States tornado climatology. *Mon. Wea. Rev.*, **116**, 495–501, https://doi.org/10.1175/1520-0493(1988)116<0495:OSIOUS>2.0.CO;2.

Edwards, R., J. T. Allen, and G. W. Carbin, 2018: Reliability and climatological impacts of convective wind estimations. *J. Appl. Meteor. Climatol.*, **57**, 1825–1845, https://doi.org/10.1175/JAMC-D-17-0306.1.

Flournoy, M. D., M. C. Coniglio, and E. N. Rasmussen, 2021: Examining relationships between environmental conditions and supercell motion in time. *Wea. Forecasting*, **36**, 737–755, https://doi.org/10.1175/WAF-D-20-0192.1.

Gaffin, D. M., 2012: The influence of terrain during the 27 April 2011 super tornado outbreak and 5 July 2012 derecho around the Great Smoky Mountains National Park. *26th Conf. on Severe Local Storms*, Nashville, TN, Amer. Meteor. Soc., P1.2, https://ams.confex.com/ams/26SLS/webprogram/Paper220492.html.

——, and S. S. Parker, 2006: A climatology of synoptic conditions associated with significant tornadoes across the southern Appalachian region. *Wea. Forecasting*, **21**, 735–751, https://doi.org/10.1175/WAF951.1.

——, and D. G. Hotz, 2011: An examination of varying supercell environments over the complex terrain of the eastern Tennessee River Valley. *Natl. Wea. Dig.*, **35**, 133–148.

Gilmore, M. S., and L. J. Wicker, 1998: The influence of midtropospheric dryness on supercell morphology and evolution. *Mon. Wea. Rev.*, **126**, 943–958, https://doi.org/10.1175/1520-0493(1998)126<0943:TIOMDO>2.0.CO;2.

Gropp, M. E., and C. E. Davenport, 2018: The impact of the nocturnal transition on the lifetime and evolution of supercell thunderstorms in the Great Plains. *Wea. Forecasting*, **33**, 1045–1061, https://doi.org/10.1175/WAF-D-17-0150.1.

Homeyer, C. R., T. N. Sandmael, C. K. Potvin, and A. M. Murphy, 2020: Distinguishing characteristics of tornadic and nontornadic supercell storms from composite mean analyses of radar observations. *Mon. Wea. Rev.*, **148**, 5015–5040, https://doi.org/10.1175/MWR-D-20-0136.1.

Houser, J. B., N. McGinnis, K. M. Butler, H. B. Bluestein, J. C. Snyder, and M. M. French, 2020: Statistical and empirical relationships between tornado intensity and both topography and land cover using rapid-scan radar observations and a GIS. *Mon. Wea. Rev.*, **148**, 4313–4338, https://doi.org/10.1175/MWR-D-19-0407.1.

Katona, B., and P. Markowski, 2021: Assessing the influence of complex terrain on severe convective environments in northeastern Alabama. *Wea. Forecasting*, **36**, 1003–1029, https://doi.org/10.1175/WAF-D-20-0136.1.

——, ——, C. Alexander, and S. Benjamin, 2016: The influence of topography on convective storm environments in the eastern United States as deduced from the HRRR. *Wea. Forecasting*, **31**, 1481–1490, https://doi.org/10.1175/WAF-D-16-0038.1.

Keighton, S., K. Kostura, and C. Liscinsky, 2004: Examination of tornadic and non-tornadic supercells in southwest Virginia on 28 April 2002. *22nd Conf. on Severe Local Storms*, Hyannis, MA, Amer. Meteor. Soc., P10.4, https://www.weather.gov/media/rnk/research/SLS_keighton_manuscript.pdf.

Knupp, K. R., and Coauthors, 2014: Meteorological overview of the devastating 27 April 2011 tornado outbreak. *Bull. Amer. Meteor. Soc.*, **95**, 1041–1062, https://doi.org/10.1175/BAMS-D-11-00229.1.

Lane, J., 2008: A comprehensive climatology of significant tornadoes in the Greenville-Spartanburg, South Carolina county warning area (1880–2006). Eastern Region Tech. Attachment 2008–01, 35 pp., https://www.weather.gov/media/erh/ta2008-01.pdf.

LaPenta, K. D., L. F. Bosart, T. J. Galarneau Jr., and M. J. Dickinson, 2005: A multiscale examination of the 31 May 1998 Mechanicville, New York, tornado. *Wea. Forecasting*, **20**, 494–516, https://doi.org/10.1175/WAF875.1.

LeBel, L. J., B. H. Tang, and R. A. Lazear, 2021: Examining terrain effects on an upstate New York tornado event utilizing a high-resolution model simulation. *Wea. Forecasting*, **36**, 2001–2020, https://doi.org/10.1175/WAF-D-21-0018.1.

Lyza, A. W., and K. Knupp, 2014: An observational analysis of potential terrain influences on tornado behavior. *27th Conf. on Severe Local Storms*, Madison, WI, Amer. Meteor. Soc., 11A.1A, https://ams.confex.com/ams/27SLS/webprogram/Paper255844.html.

——, T. A. Murphy, B. T. Goudeau, P. T. Pangle, K. R. Knupp, and R. A. Wade, 2020: Observed near-storm environment variations across the southern Cumberland Plateau system in northeastern Alabama. *Mon. Wea. Rev.*, **148**, 1465–1482, https://doi.org/10.1175/MWR-D-19-0190.1.

Markowski, P. M., 2002: Hook echoes and rear-flank downdrafts: A review. *Mon. Wea. Rev.*, **130**, 852–876, https://doi.org/10.1175/1520-0493(2002)130<0852:HEARFD>2.0.CO;2.

——, and N. Dotzek, 2011: A numerical study of the effects of orography on supercells. *Atmos. Res.*, **100**, 457–478, https://doi.org/10.1016/j.atmosres.2010.12.027.

McKeown, K. E., 2021: Radar characteristics of observed supercells interacting with the Appalachian Mountains. M.S. thesis, Dept. of Geography and Earth Sciences, University of North Carolina at Charlotte, 131 pp.

Mulholland, J. P., S. W. Nesbitt, and R. J. Trapp, 2019: A case study of terrain influences on upscale convective growth of a supercell. *Mon. Wea. Rev.*, **147**, 4305–4324, https://doi.org/10.1175/MWR-D-19-0099.1.

——, ——, ——, and J. M. Peters, 2020: The influence of terrain on the convective environment and associated convective morphology from an idealized modeling perspective. *J. Atmos. Sci.*, **77**, 3929–3949, https://doi.org/10.1175/JAS-D-19-0190.1.

Murillo, E. M., and C. R. Homeyer, 2019: Severe hail fall and hailstorm detection using remote sensing observations. *J. Appl. Meteor. Climatol.*, **58**, 947–970, https://doi.org/10.1175/JAMC-D-18-0247.1.

Prociv, K. A., 2012: Terrain and landcover effects of the southern Appalachian Mountains on the rotational low-level wind fields of supercell thunderstorms. M.S. thesis, Dept. of Geography, Virginia Polytechnic Institute and State University, 95 pp.

Purpura, S. M., C. E. Davenport, M. D. Eastin, K. E. McKeown, and R. R. Riggin, 2023: Environmental evolution of supercell thunderstorms interacting with the Appalachian Mountains. *Wea. Forecasting*, **38**, 179–198, https://doi.org/10.1175/WAF-D-22-0115.1.

Rinehart, R. E., and A. Borho, 1993: A comparison of the detectability of microbursts in Orlando, Florida, by two C-band Doppler radars. *J. Appl. Meteor.*, **32**, 476–489, https://doi.org/10.1175/1520-0450(1993)032<0476:ACOTDO>2.0.CO;2.

Rotunno, R., and J. Klemp, 1985: On the rotation and propagation of simulated supercell thunderstorms. *J. Atmos. Sci.*, **42**, 271–292, https://doi.org/10.1175/1520-0469(1985)042<0271:OTRAPO>2.0.CO;2.

Scheffknecht, P., S. Serafin, and V. Grubišić, 2017: A long-lived supercell over mountainous terrain. *Quart. J. Roy. Meteor. Soc.*, **143**, 2973–2986, https://doi.org/10.1002/qj.3127.

Schneider, D. G., 2009: The impact of terrain on three cases of tornadogenesis in the Great Tennessee Valley. *Electron. J. Oper. Meteor.*, **10**, 1–33.

Schultz, C. J., L. D. Carey, E. V. Schultz, and R. J. Blakeslee, 2015: Insight into the kinematic and microphysical processes that control lightning jumps. *Wea. Forecasting*, **30**, 1591–1621, https://doi.org/10.1175/WAF-D-14-00147.1.

Sessa, M. F., and R. J. Trapp, 2020: Observed relationship between tornado intensity and pretornadic mesocyclone characteristics. *Wea. Forecasting*, **35**, 1243–1261, https://doi.org/10.1175/WAF-D-19-0099.1.

Sherburn, K. D., and M. D. Parker, 2014: Climatology and ingredients of significant severe convection in high-shear, low-CAPE environments. *Wea. Forecasting*, **29**, 854–877, https://doi.org/10.1175/WAF-D-13-00041.1.

Smith, G. M., Y.-L. Lin, and Y. Rastigejev, 2016: Orographic effects on supercell: Development and structure, intensity and tracking. *Environ. Nat. Resour. Res.*, **6**, 76–91, https://doi.org/10.5539/enrr.v6n2p76.

Stewart, S. R., 1991: The prediction of pulse-type thunderstorm gusts using vertically integrated liquid water content (VIL) and the cloud top penetrative downdraft mechanism. NOAA Tech. Memo. NWS SR-136, 24 pp., https://repository.library.noaa.gov/view/noaa/7204.

Tang, B., M. Vaughan, R. Lazear, K. Corbosiero, L. Bosart, T. Wasula, I. Lee, and K. Lipton, 2016: Topographic and boundary influences on the 22 May 2014 Duanesburg, New York, tornadic supercell. *Wea. Forecasting*, **31**, 107–127, https://doi.org/10.1175/WAF-D-15-0101.1.

Thompson, R. L., C. M. Mead, and R. Edwards, 2007: Effective storm-relative helicity and bulk shear in supercell thunderstorm environments. *Wea. Forecasting*, **22**, 102–115, https://doi.org/10.1175/WAF969.1.

Trapp, R. J., G. J. Stumpf, and K. L. Manross, 2005: A reassessment of the percentage of tornadic mesocyclones. *Wea. Forecasting*, **20**, 680–687, https://doi.org/10.1175/WAF864.1.

——, D. M. Wheatley, N. T. Atkins, R. W. Przybylinski, and R. Wolf, 2006: Buyer beware: Some words of caution on the use of severe wind reports in postevent assessment and research. *Wea. Forecasting*, **21**, 408–415, https://doi.org/10.1175/WAF925.1.

Wakimoto, R. M., and V. N. Bringi, 1988: Dual-polarization observations of microbursts associated with intense convection: The 20 July storm during the MIST project. *Mon. Wea. Rev.*, **116**, 1521–1539, https://doi.org/10.1175/1520-0493(1988)116<1521:DPOOMA>2.0.CO;2.

Wilks, D. S., 2006: *Statistical Methods in the Atmospheric Sciences*. 2nd ed. Academic Press, 648 pp.

Witt, A., M. D. Eilts, G. J. Stumpf, J. T. Johnson, E. D. W. Mitchell, and K. W. Thomas, 1998: An enhanced hail detection algorithm for the WSR-88D. *Wea. Forecasting*, **13**, 286–303, https://doi.org/10.1175/1520-0434(1998)013<0286:AEHDAF>2.0.CO;2.

Wunsch, M. S., and M. M. French, 2020: Delayed tornadogenesis within New York State severe storms. *J. Oper. Meteor.*, **8**, 79–92, https://doi.org/10.15191/nwajom.2020.0806.